

## Mixed Layer Heat Balance on Intraseasonal Time Scales in the Northwestern Tropical Atlantic Ocean\*

GREGORY R. FOLTZ AND MICHAEL J. MCPHADEN

*NOAA/Pacific Marine Environmental Laboratory, Seattle, Washington*

(Manuscript received 3 January 2005, in final form 25 April 2005)

### ABSTRACT

Recent observations have shown evidence of intraseasonal oscillations (with periods of approximately 1–2 months) in the northern and southern tropical Atlantic trade winds. In this paper, the oceanic response to the observed intraseasonal wind variability is addressed through an analysis of the surface mixed layer heat balance, focusing on three locations in the northwestern tropical Atlantic where in situ measurements from moored buoys are available (14.5°N, 51°W; 15°N, 38°W; and 18°N, 34°W). It is found that local heat storage at all three locations is balanced primarily by wind-induced latent heat loss, which is the same mechanism that is believed to play a dominant role on interannual and decadal time scales in the region. It is also found that the intraseasonal wind speed oscillations are linked to changes in surface wind convergence and convection over the western equatorial Atlantic warm pool. These atmospheric circulation anomalies and wind-induced SST anomalies potentially feed back on one another to affect longer time-scale variability in the region.

### 1. Introduction

The climate of the tropical Atlantic undergoes significant fluctuations on time scales ranging from seasonal to decadal. In contrast to the tropical Pacific, however, in which variability is concentrated close to the equator, the tropical Atlantic supports a mode of variability that extends into the subtropics, affecting sea surface temperatures (SSTs) and surface winds in both hemispheres (Nobre and Shukla 1996). While coupled ocean–atmosphere interactions internal to the tropical Atlantic seem to contribute to some of the observed variability (Chang et al. 1997), it appears that external forcing from the equatorial Pacific and the extratropical Atlantic also plays a significant role (Xie and Tanimoto 1998; Czaja et al. 2002).

One of the regions where external forcing is likely to be important is the northern tropical Atlantic, where

variations in surface wind speed are strongly correlated with latent heat loss and local heat storage (Cayan 1992; Enfield and Mayer 1997). The trade winds in the northern tropical Atlantic exhibit a strong seasonal cycle, with maximum strength in boreal winter and a minimum in boreal fall (Fig. 1a). These winds also exhibit considerable intraseasonal variability, particularly in the 40–70-day period band (Fig. 1b). In a recent study, Foltz and McPhaden (2004) investigated these fluctuations in wind speed, focusing on their surface atmospheric structure from a combination of satellite and reanalysis data. They showed that there is a peak in the intraseasonal percent variance in the northern tropical Atlantic and that the oscillations in this region are significantly correlated with both the North Atlantic Oscillation and the Madden–Julian oscillation (MJO) in the tropical Indo-Pacific.

The intraseasonal wind speed fluctuations in the northern tropical Atlantic are also strongly negatively correlated with the local SST when wind speed leads by about two weeks (Czaja and Thompson 2004; Foltz and McPhaden 2004). Here we examine the causes of these intraseasonal SST fluctuations through an observational analysis of the oceanic mixed layer heat balance, focusing on data from three moored buoys in the northwestern tropical Atlantic where the intraseasonal wind speed signal is strong.

---

\* Pacific Marine Environmental Laboratory Contribution Number 2780.

---

*Corresponding author address:* Dr. Gregory R. Foltz, NOAA/Pacific Marine Environmental Laboratory, 7600 Sand Point Way NE, Seattle, WA 98115.  
E-mail: gregory.foltz@noaa.gov

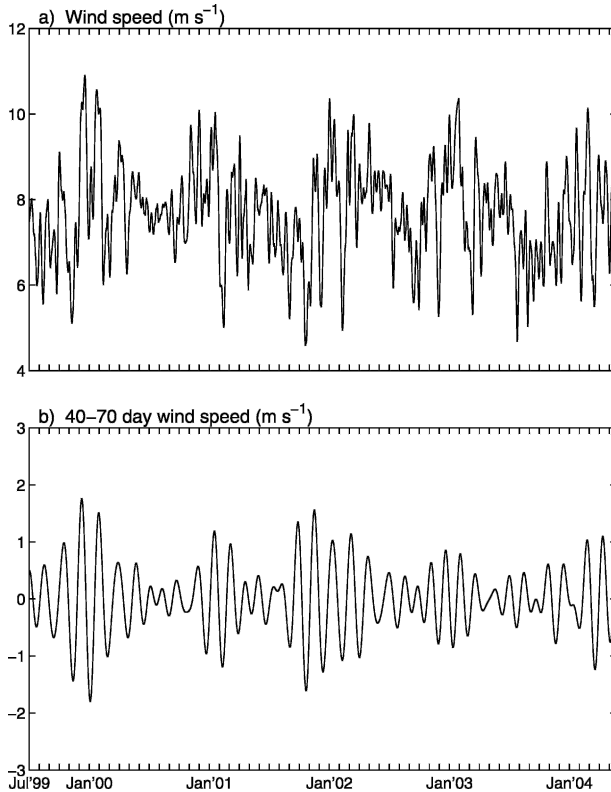


FIG. 1. (a) Daily QuikSCAT wind speed, smoothed with a 5-day running mean filter and averaged over the North Atlantic (NATL) index region (defined as 12–22°N, 55–25°W; see Fig. 2a). (b) Wind speed as in (a), but bandpass filtered to retain variability only in the 40–70-day period range.

## 2. Data and methods

### a. Datasets

We use a combination of satellite data and measurements from three moored buoys in the northwestern tropical Atlantic (Fig. 2) to estimate various terms in the surface mixed layer heat balance (described in detail in section 2b). One of the buoys is the northernmost moored buoy of the Pilot Research Array in the Tropical Atlantic (PIRATA; Servain et al. 1998) located at 15°N, 38°W. The buoy measures subsurface temperature and salinity, air temperature, relative humidity, wind velocity, shortwave radiation (SWR), and precipitation. Ocean temperature is measured at 11 depths between 1 (i.e., bulk SST) and 500 m, with 20-m spacing in the upper 140 m, while salinity is measured at 1 [sea surface salinity (SSS)], 20, 40, and 120 m. Air temperature and relative humidity are measured at a height of 3 m above sea level, shortwave radiation and rainfall are measured at 3.5 m, and wind velocity is measured at 4 m.

The sampling interval is 10 min for all data except shortwave radiation, which is sampled at 2-min inter-

vals, and rainfall, which is sampled at 1-min intervals. Daily averages are transmitted to shore in real time, while the high temporal resolution data are internally recorded. Here we use both the high-resolution data (10-min samples or 10-min means for rain and radiation) and the daily averaged data for the time period 1999–2004.

We use surface measurements from a moored buoy of the Northwest Tropical Atlantic Station for air–sea flux measurement (NTAS), located at 14.5°N, 51°W. Available measurements include bulk SST (measured at a depth of 1.7 m), air temperature, relative humidity, wind velocity, shortwave radiation, barometric pressure, and precipitation (all measured at heights between 2.5 and 3.5 m). Hourly data are available for the period March 2001–February 2004. We use both the quality-controlled data (available for March 2001–February 2003) and the real-time data (February 2003–February 2004). We compared the record-length means and standard deviations of the real-time data for February 2003–February 2004 to those of the quality-controlled data and found that they are similar. We therefore use the real-time data for February 2003–February 2004 without any corrections.

We also use measurements from the southwestern moored buoy of the Subduction Experiment, located at 18°N, 34°W. The buoy-measured subsurface temperature and horizontal velocity, bulk SST (measured at a depth of 1 m), air temperature, relative humidity, wind velocity, shortwave radiation, incoming longwave radiation, barometric pressure, and precipitation (all measured at heights between 2 and 3 m) during June 1991–June 1993. Ocean temperature was measured with 20-m spacing between 10 and 50 m and with 10-m spacing between 50 and 100 m, while subsurface ocean velocity was measured with 20-m spacing between 10 and 110 m. The data are available at 15-min intervals, and we averaged these to daily means except for the computation of surface fluxes as described below. Gaps in the surface records (mainly during November 1991–February 1992 and June–July 1992) were filled with 4-times-daily output from the European Centre for Medium-Range Weather Forecasts (ECMWF) model. Gaps in the subsurface temperature and velocity data (November 1991–February 1992 and June–October 1992) were not filled. Figure 3 shows the temporal coverage of each variable at the PIRATA, NTAS, and Subduction moorings.

We use the monthly climatological mixed layer depth ( $h$ ) and isothermal layer depth (ILD) estimates of Monterey and Levitus (1997), which are available on a  $1^\circ \times 1^\circ$  grid. They are based on subsurface temperature and salinity from the *World Ocean Atlas 1994* and are

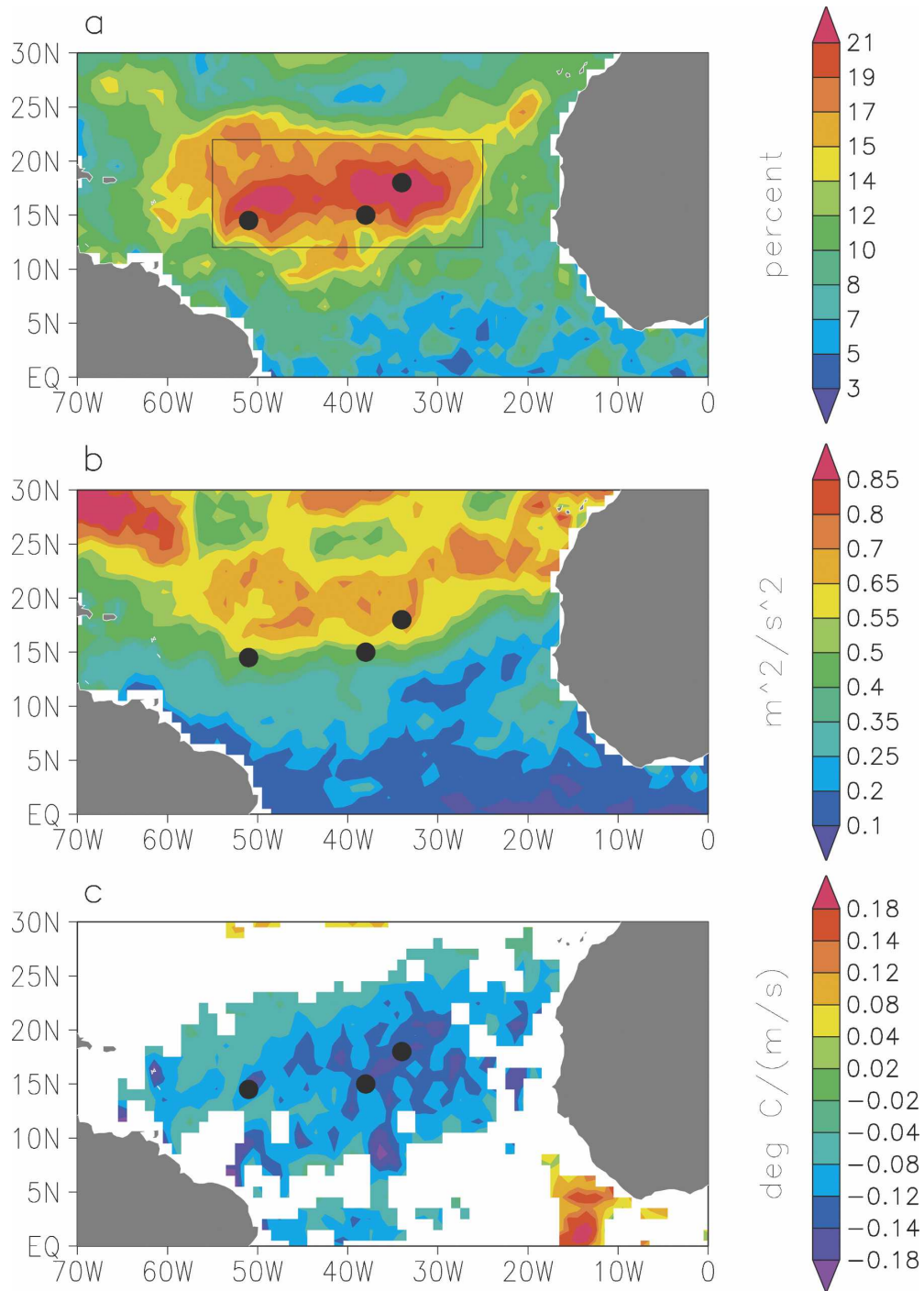


FIG. 2. (a) Percentage of the daily QuikSCAT wind speed variance (1999–2004) in the 40–70-day band. A daily mean seasonal cycle has been removed prior to calculation of the variance. The rectangle encloses the region ( $12^{\circ}$ – $22^{\circ}$ N,  $55^{\circ}$ – $25^{\circ}$ W) used to form the 40–70-day NATL wind speed index. Note that we have changed the index region slightly from that used by Foltz and McPhaden (2004;  $15^{\circ}$ – $25^{\circ}$ N,  $50^{\circ}$ – $20^{\circ}$ W), which was based on a 20-yr record of NCEP–NCAR reanalysis wind speed, in order to maximize the intraseasonal signals for the QuikSCAT time period. (b) QuikSCAT wind speed variance in the 40–70-day band. (c) The 40–70-day TMI SST regressed onto the NATL wind speed index. SST was regressed with a 14-day lag (i.e., SST lags the wind speed index by  $\sim$  one-quarter of a cycle). Values are shown only where they exceed the 90% confidence level. Numbers of degrees of freedom are estimated following Davis (1976). Black dots indicate the positions of the moored buoys used in this study.

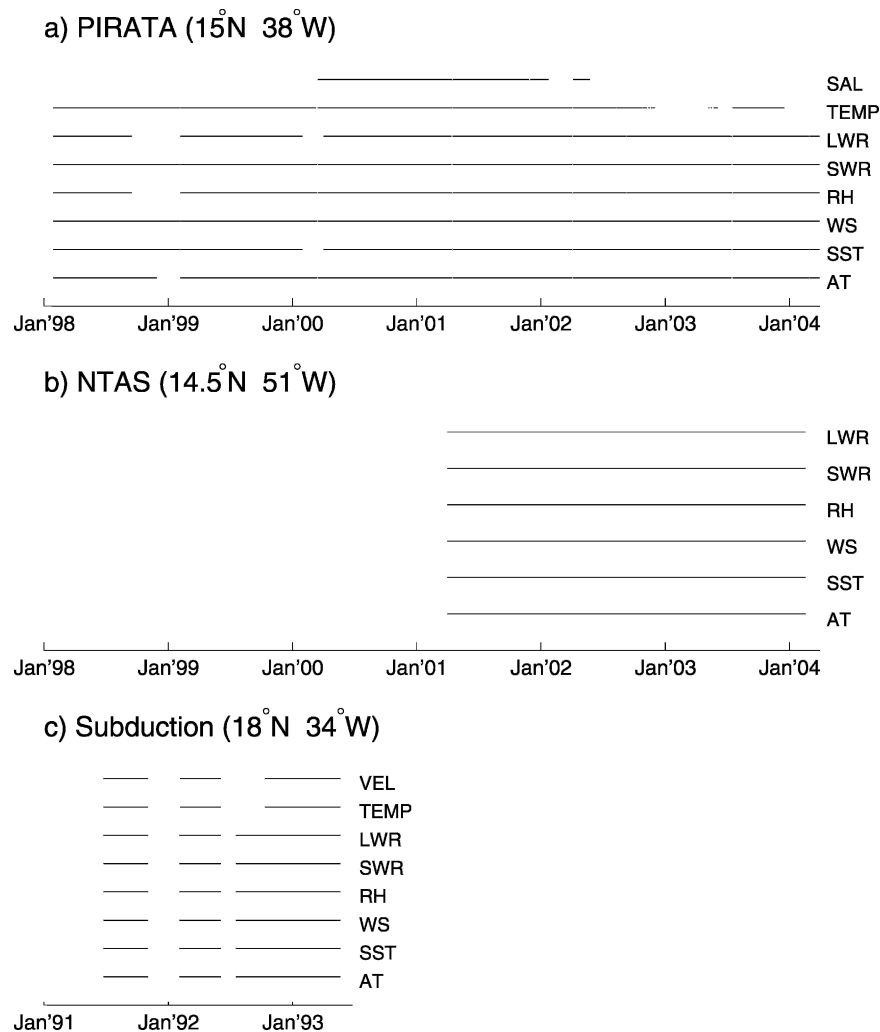


FIG. 3. Availability of air temperature (AT), SST, wind speed (WS), relative humidity (RH), shortwave radiation (SWR), longwave radiation (LWR), subsurface temperature (TEMP), salinity (SAL), and ocean velocity (VEL) at (a) the PIRATA mooring, (b) the NTAS mooring, and (c) the Subduction mooring. TEMP, SAL, and VEL are measured at multiple depths (see text for discussion).

defined using the criterion of a  $0.125 \text{ kg m}^{-3}$  density increase from the surface for  $h$  and a  $0.5^\circ\text{C}$  temperature decrease from the surface for the ILD. The vertical resolution of the temperature and salinity data used to estimate  $h$  and ILD is 10 m between the surface and 30 m, and 25 m between 50 and 200 m.

We also use satellite-based estimates of SST, rainfall, wind velocity, and sea level. SST is obtained from the Tropical Rainfall Measuring Mission (TRMM) Microwave Imager (TMI), while rainfall is obtained from the TRMM Microwave Imager and precipitation radar. Both are available on a  $0.5^\circ \times 0.5^\circ \times$  daily grid beginning December 1997 (Wentz 1997). Surface wind velocity is obtained from the SeaWinds scatterometer onboard the QuikSCAT satellite, available on a  $0.25^\circ \times$

$0.25^\circ \times$  daily grid beginning July 1999 (Liu et al. 1998), and from the Special Sensor Microwave Imager (SSM/I) on the Defense Meteorological Satellite Program (DMSP) satellites, available on a  $1^\circ \times 1^\circ \times 5$ -day grid during 1987–2001. We have regridded the TMI SST/rainfall and the QuikSCAT wind velocity data to a  $1^\circ \times 1^\circ$  grid and interpolated the SSM/I wind velocity data to a daily resolution.

We have obtained sea level data from the TOPEX/Poseidon and Jason altimeters (Cheney et al. 1994) for the time period 1992–2004 in order to estimate geostrophic mixed layer ocean velocity at the NTAS and PIRATA sites, where direct velocity measurements are not available. These currents are combined with Ekman currents in order to estimate the total mixed layer

velocity. The along-track sea level data are mapped to a  $1^\circ \times 1^\circ \times 10$ -day grid using a Gaussian spatial weighting function ( $\exp\{-0.7\{(\Delta\text{lat})^2 + [\cos(\text{lat})\Delta\text{lon}]^2/4\}\}$ ) and then interpolated to a daily resolution. In this expression,  $\Delta\text{lat}$  and  $\Delta\text{lon}$  are distance in latitude and longitude from a given data point. The 1993–96 mean sea level is used as a proxy for the geoid + climatological sea level and is removed and replaced with a mean dynamic height surface (relative to 1000 m) obtained from the climatological gridded  $1^\circ \times 1^\circ$  temperature and salinity fields of Levitus et al. (1994) and Levitus and Boyer (1994). We have compared geostrophic velocities from these sea level estimates to those derived from the Archiving, Validation, and Interpretation of Satellite Oceanographic data (AVISO) sea level estimates, which include the 7-yr mean Enact dynamic topography (Rio and Hernandez 2004) and found that they are similar (at all sites, cross correlations are 0.7–0.8 and rms differences are 3–5  $\text{cm s}^{-1}$  for 2001–04, when the AVISO currents are available).

Finally, we use three longer datasets for comparison with the corresponding shorter-duration satellite-based measurements described above. These include the Climate Prediction Center (CPC) Merged Analysis of Precipitation (CMAP) on a  $2.5^\circ \times 2.5^\circ \times 5$ -day grid, Reynolds et al. (2002) SST on a  $1^\circ \times 1^\circ \times$  weekly grid, and National Centers for Environmental Prediction–National Center for Atmospheric Research (NCEP–NCAR) reanalysis (Kalnay et al. 1996) surface wind velocity on a  $2^\circ \times 2^\circ \times$  daily grid. We have interpolated the precipitation and SST data to a daily resolution. All datasets are available during 1982–2004.

### b. Mixed layer heat equation

Following Stevenson and Niiler (1983) and Moisan and Niiler (1998), the mixed layer heat balance can be written as

$$h \frac{\partial T}{\partial t} + h\mathbf{v} \cdot \nabla T + H\Delta T w_e + \nabla \cdot \int_{-h}^0 \hat{\mathbf{v}} \hat{T} dz = \frac{q_0 - q_{-h}}{\rho c_p}. \quad (1)$$

The terms represent, from left to right, local storage, horizontal advection, entrainment, vertical temperature/velocity covariance, net surface heat flux adjusted for the penetration of light below the mixed layer ( $q_0$ ), and vertical turbulent diffusion at the base of the mixed layer ( $q_{-h}$ ). Here  $h$  is the depth of the mixed layer;  $T$  and  $\mathbf{v}$  are temperature and velocity, respectively, vertically averaged from the surface to a depth of  $-h$ ;  $\hat{T}$  and  $\hat{\mathbf{v}}$  are deviations from the vertical average;  $H$  is the Heaviside unit function; and  $\Delta T = T - T_{-h}$ . Entrainment velocity can be rewritten as  $w_e = \partial h / \partial t + \nabla \cdot h\mathbf{v}$  following Stevenson and Niiler (1983) and is associated

with a mass flux that crosses the base of the mixed layer. We neglect the vertical temperature difference/velocity shear covariance term and  $q_{-h}$  since we cannot reliably estimate it. Swenson and Hansen (1999) estimate that the covariance term is  $<10\%$  as large as the other terms in (1), while the results of Foltz et al. (2003) suggest that  $q_{-h}$  is insignificant on seasonal time scales.

To emphasize variability on intraseasonal time scales, we bandpass filter all terms in (1) using a trapezoidal filter with corner periods of 40, 45, 65, and 70 days (all variance  $<40$  days and  $>70$  days is removed, and all variance between 45 and 65 days is retained). Missing data are replaced with the time series mean prior to filtering and are left blank after filtering. In a previous study, Foltz and McPhaden (2004) used a spectral window of 30–70 days to describe intraseasonal variability in the northern and southern tropical Atlantic. Here we have narrowed the spectral window to 40–70 days on the basis of the wind speed spectra at the three buoy locations (Fig. 4).

We begin by considering the effects of surface flux terms on local heat storage in (1). We start with surface fluxes since we anticipate that they will contribute significantly to the heat budget based on the seasonal analysis of Foltz et al. (2003) and because we can estimate the largest of the surface flux terms with a high degree of reliability. The horizontal advection and vertical entrainment terms, which we anticipate will be smaller in magnitude and contain a higher degree of uncertainty, will be considered in a later section.

First we consider the local storage term [first term in (1)]. The time rate of change of mixed layer temperature ( $\partial T / \partial t$ ) is estimated using bulk SST from the buoys since there are gaps in the subsurface temperature data (Fig. 3). A comparison of daily SST and  $T$  at  $15^\circ\text{N}$ ,  $38^\circ\text{W}$  (using either a temperature- or density-based mixed layer depth as defined later in this section) reveals a cross correlation of nearly one and an rms scatter of  $0.1^\circ\text{C}$ , suggesting that SST is a good proxy for  $T$ . Gaps in the buoy SST record at  $15^\circ\text{N}$ ,  $38^\circ\text{W}$  (Fig. 3) are filled with TMI SST since TMI SST agrees reasonably well with the buoy SST (the cross correlation is nearly one and the daily rms scatter is  $0.3^\circ\text{C}$ ).

The mixed layer depth,  $h$ , which contributes to the storage term in (1), is affected by the vertical distributions of both temperature and salinity. Throughout much of the open upper ocean, density is controlled primarily by temperature. However, the northwestern tropical Atlantic is affected by strong river discharge and salinity fronts that influence the near-surface stratification and hence the mixed layer depth (Pailler et al. 1999). The barrier layer thickness (defined as the difference between the ILD and the true mixed layer

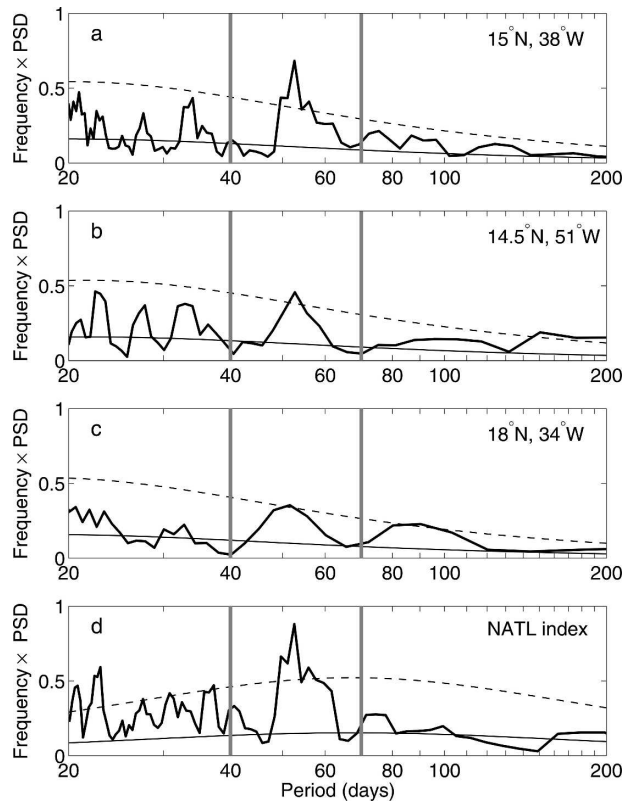


FIG. 4. Normalized power spectra of wind speed from (a) the PIRATA buoy at  $15^{\circ}\text{N}$ ,  $38^{\circ}\text{W}$  (1999–2004); (b) the NTAS buoy at  $14.5^{\circ}\text{N}$ ,  $51^{\circ}\text{W}$  (2001–04); (c) the southwestern Subduction buoy at  $18^{\circ}\text{N}$ ,  $34^{\circ}\text{W}$  (1991–93); and (d) from QuikSCAT, averaged over the NATL index region (Fig. 2a). Spectra are shown in variance-preserving plots [frequency  $\times$  power spectral density (PSD)]. Solid black lines represent red noise spectra based on a lag-1 autoregressive process. Dashed lines represent the 80% confidence level of a chi-square distribution. Vertical gray lines indicate periods of 40 and 70 days.

depth,  $h$ ) averages 40 m at  $14.5^{\circ}\text{N}$ ,  $51^{\circ}\text{W}$  and can exceed 80% of the isothermal layer depth (Fig. 5b). The thick barrier layer at this location is due to the combination of northwestward advection of Amazon River outflow and subduction and southwestward advection of high-salinity waters originating in the subtropical north Atlantic (Sprintall and Tomczak 1992; Pailler et al. 1999). The barrier layer thickness is less significant at  $15^{\circ}\text{N}$ ,  $38^{\circ}\text{W}$  and  $18^{\circ}\text{N}$ ,  $34^{\circ}\text{W}$  (10–20 m on average) but still spans 15%–50% of the ILD during boreal fall and winter based on the Monterey and Levitus (1997, hereafter ML97) climatology (Figs. 5a,c).

The direct estimation of  $h$  at the buoys is hindered by a lack of subsurface salinity at the NTAS and Subduction moorings and significant gaps in the PIRATA salinity record (Fig. 3). For this reason we use a combination of buoy-based estimates of  $h$  and ILD and climatological  $h$  from ML97 as described below.

At the PIRATA site ( $15^{\circ}\text{N}$ ,  $38^{\circ}\text{W}$ ), we estimate  $h$  from concurrent buoy subsurface temperature and salinity measurements based on a  $0.125 \text{ kg m}^{-3}$  density criterion following the procedure of Foltz et al. (2004). To address the problem of gaps, we form a climatological mixed layer depth (using data mainly from 2000–01) and repeat it for each year, thus eliminating intraseasonal and interannual variations of  $h$ . Daily subsurface temperature and salinity data from 2000–01 (nonclimatological) indicate that intraseasonal variations of  $h$  are weak (the standard deviation of the 40–70-day  $h$  is  $<15\%$  of the annual mean  $h$ ). Interannual variations of  $h$  are more difficult to estimate based on the available data. We have found that they are weak during 2000–01 (annual mean  $h$  is 44 and 45 m for 2000 and 2001, respectively), but they may be important during other years. We have found that our PIRATA-based climatological  $h$  is consistently shallower than the ML97  $h$  (Fig. 5a). The difference is most likely due to differences in the vertical resolution of the salinity measurements (the ML97 estimates include high-vertical-resolution measurements from conductivity–temperature–depth (CTD) casts, while the PIRATA-based estimates suffer from a lack of salinity measurements between 40 and 120 m). We therefore correct the PIRATA-based estimates of  $h$  by subtracting the mean seasonal cycle of the difference between the PIRATA  $h$  and the ML97  $h$ .

Since neither subsurface temperature nor salinity is available from the NTAS mooring, we use the climatological ML97  $h$  and repeat it for each year. At  $18^{\circ}\text{N}$ ,  $34^{\circ}\text{W}$ , where subsurface temperature data are available from the buoy, but salinity data are not, we regress the ML97 mixed layer depth onto the ML97 ILD and use the regression coefficients to estimate a daily mixed layer depth from the buoy ILD. Since the resulting time series contains significant gaps, we form a daily climatology and repeat it for each year. As at  $15^{\circ}\text{N}$ ,  $38^{\circ}\text{W}$ , intraseasonal variations of  $h$  at  $18^{\circ}\text{N}$ ,  $34^{\circ}\text{W}$  are small ( $<10\%$  of the annual mean  $h$ ).

Next we consider the surface heat flux, which consists of latent and sensible heat loss, shortwave radiation absorbed in the mixed layer, and net longwave radiation emitted from the sea surface. Latent and sensible heat loss are estimated from the Coupled Ocean–Atmosphere Response Experiment (COARE) bulk flux algorithm (Fairall et al. 1996), using buoy estimates of SST, air temperature, relative humidity, and wind speed. We have compared latent and sensible heat loss terms estimated with high-resolution data (10-min, hourly, and 15-min for PIRATA, NTAS, and Subduction, respectively) to those based on daily data and found that they are nearly identical at each location

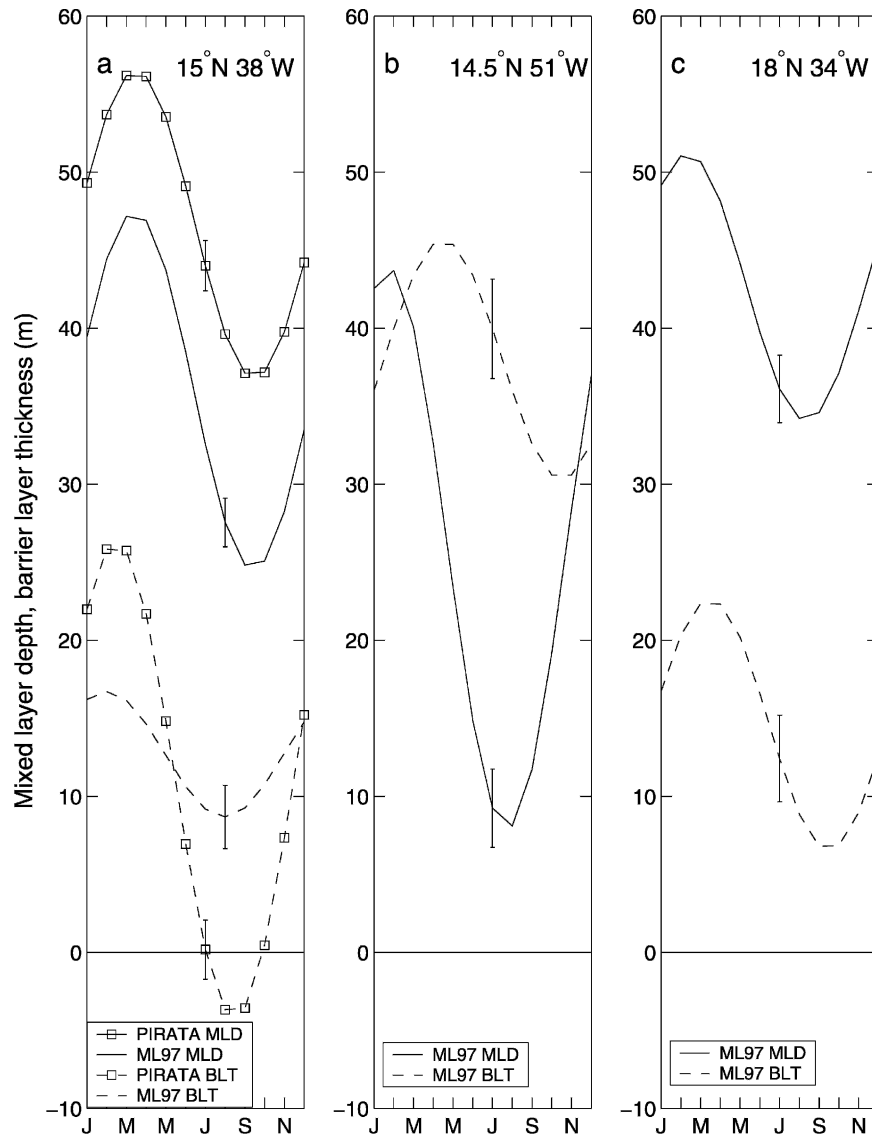


FIG. 5. Monterey and Levitus (1997) mixed layer depth (based on a  $0.125 \text{ kg m}^{-3}$  criterion; solid lines) and barrier layer thickness [defined as the difference between the isothermal layer depth (based on a  $0.5^\circ\text{C}$  criterion) and the mixed layer depth; dashed lines] at (a)  $15^\circ\text{N}$ ,  $38^\circ\text{W}$ ; (b)  $14.5^\circ\text{N}$ ,  $51^\circ\text{W}$ ; and (c)  $18^\circ\text{N}$ ,  $34^\circ\text{W}$ . Also shown in (a) are the PIRATA-based mixed layer depth (solid line with squares) and barrier layer thickness (dashed line with squares). Monthly time series have been linear least squares fitted to annual mean + annual and semiannual harmonics. Error bars denote one standard error based on residuals to the fits, assuming 7 degrees of freedom.

(differences in the record-length means and standard deviations of the daily-averaged values are  $<0.3$  and  $<0.1 \text{ W m}^{-2}$ , respectively, for both latent and sensible heat loss). We therefore use the daily data, which contain fewer gaps, to estimate the latent and sensible fluxes at each location.

The net surface shortwave radiation is available directly from the moorings, assuming an albedo of 6%. Following Wang and McPhaden (1999), we model the

amount of shortwave radiation penetrating the mixed layer as  $Q_{\text{pen}} = 0.47Q_{\text{surf}}e^{-0.04h}$ , where  $Q_{\text{surf}}$  is the surface shortwave radiation and  $h$  is the depth of the mixed layer. Based on the analysis of Medovaya et al. (2002), we expect that aerosol buildup on the shortwave radiation sensors, caused by the westward advection of dust from the Sahara Desert, may cause shortwave radiation measurement errors at all locations. Indeed, the shortwave radiation record from the

PIRATA buoy shows discontinuous jumps of up to  $50 \text{ W m}^{-2}$  immediately following periods when the buoy was serviced and the radiometer was cleaned. We note that Waliser et al. (1999) also found a significant shortwave radiation bias ( $>70 \text{ W m}^{-2}$ , with the buoy estimates lower) at the southeast Subduction buoy site ( $18^\circ\text{N}$ ,  $22^\circ\text{W}$ ) that they partially attributed to the build-up of Saharan dust on the shortwave radiation sensor.

We estimate the magnitude of each shortwave radiation jump at the PIRATA site as the difference in shortwave radiation between the 10-day average following the buoy replacement and the 10-day average before the replacement. We then eliminate all jumps in the record by adding a linear trend to each period between jumps on the assumption that the average shortwave radiation between adjacent 10-day periods should be nearly identical. The standard deviations of the original and corrected 40–70-day bandpass-filtered shortwave radiation measurements are similar ( $8.5$  and  $8.3 \text{ W m}^{-2}$ , respectively), and the time series have a correlation coefficient of  $0.9$ , suggesting that the discontinuous jumps do not significantly affect the intraseasonal signal. We did not identify any discontinuities in the NTAS and Subduction shortwave radiation records, and we have therefore not applied any corrections to these data.

Following Cronin and McPhaden (1997), we estimate the net longwave radiation emission at  $14.5^\circ\text{N}$ ,  $51^\circ\text{W}$  and  $15^\circ\text{N}$ ,  $38^\circ\text{W}$  from the Clark et al. (1974) bulk formula:

$$Q_{\text{lw}} = \epsilon\sigma T_s^4(0.39 - 0.05e_a^{1/2})(1 - 0.51C^2) + 4\epsilon\sigma T_s^3(T_s - T_{\text{air}}),$$

where  $\epsilon = 0.97$  is the emissivity,  $\sigma$  is the Stephan-Boltzmann constant,  $T_{\text{air}}$  is the surface air temperature,  $e_a$  is the surface vapor pressure,  $T_s$  is SST, and  $C$  is the cloud cover index. We use buoy measurements of SST, air temperature, and relative humidity and estimate cloudiness by inverting Reed's (1977) expression for the daily averaged insolation:

$$C = 1.61 \left( 1 - \frac{Q_{\text{sw}}}{Q_{\text{cs}}} + 0.0019n \right),$$

where  $Q_{\text{sw}}$  is the daily-averaged surface shortwave radiation measured at the buoys,  $Q_{\text{cs}}$  is the clear-sky radiation, and  $n$  is the noontime solar altitude. Results based on daily and 10-min SST, air temperature, relative humidity, and  $C$  (we form 10-min values of  $C$  from interpolation of the daily average values) are similar at both locations. Standard deviations of the 40–70-day bandpassed data are within  $0.5 \text{ W m}^{-2}$  at both locations, and correlations between 10-min and daily values

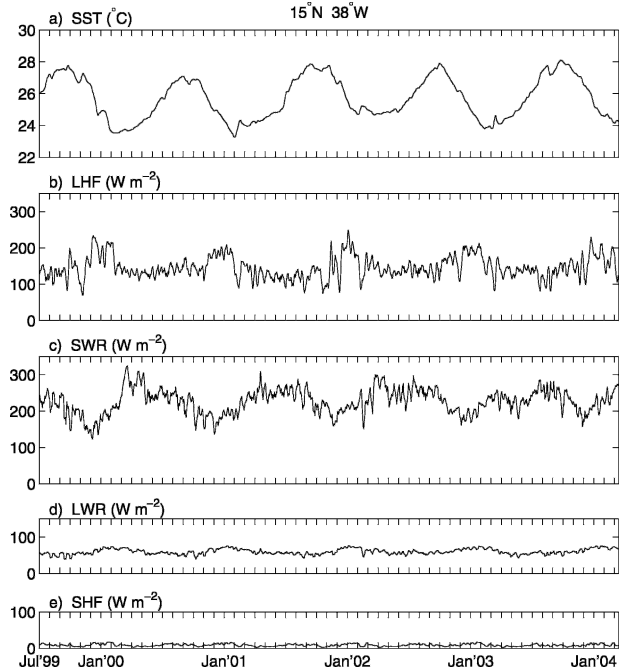


FIG. 6. Daily measurements from the PIRATA mooring, smoothed with a 5-day running mean filter: (a) SST, (b) LHF, (c) SWR, (d) net longwave radiation, and (e) sensible heat flux (latent, longwave, and sensible heat fluxes were estimated from bulk formulas, with values  $>0$  indicating heat loss from the ocean).

are  $0.9$  at both locations. We therefore use daily estimates of SST, air temperature, relative humidity, and shortwave radiation to estimate the net longwave radiation emission at both sites.

At  $18^\circ\text{N}$ ,  $34^\circ\text{W}$ , incoming longwave radiation is measured directly at the buoy. We therefore estimate the net longwave radiation emission at this location as  $Q_{\text{lw}} = \epsilon\sigma T_s^4 - Q_0$ , where  $Q_0$  is the incoming longwave radiation. The record-length means of daily measured and modeled  $Q_0$  are  $380$  and  $365 \text{ W m}^{-2}$ , respectively, and the rms difference between the measured and modeled values is  $20 \text{ W m}^{-2}$ , which is within the  $15$ – $20 \text{ W m}^{-2}$  accuracy of the radiometer (Moyer and Weller 1997). The standard deviations of the measured and modeled 40–70-day  $Q_0$  are  $2.5$  and  $2.2 \text{ W m}^{-2}$ , respectively, and the cross correlation is  $0.6$ , which is significant at the  $95\%$  level.

### 3. Local heat balance

The daily mean records of SST and latent heat loss at  $15^\circ\text{N}$ ,  $38^\circ\text{W}$  reveal strong seasonal cycles as well as significant intraseasonal variability (Fig. 6). The largest and most highly variable terms are shortwave radiation and latent heat flux (LHF). Bandpassed versions of these data at all three locations indicate that intraseasonal

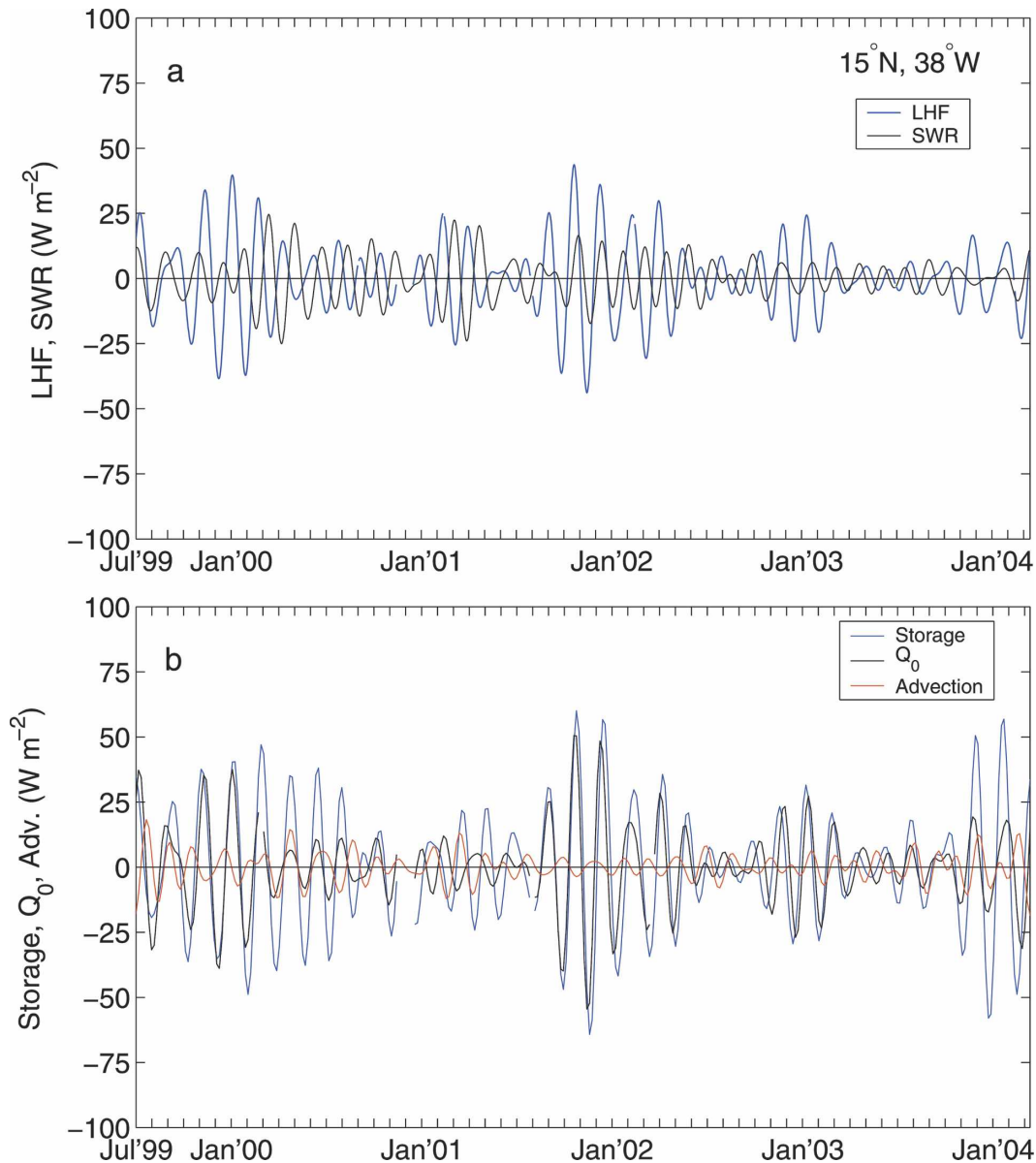


FIG. 7. Mixed layer heat budget at 15°N, 38°W. (a) The 40–70-day bandpass-filtered LHF and absorbed SWR. (b) Local heat storage, surface heat flux (latent + shortwave + longwave + sensible), and horizontal advection.

variations in heat storage are most strongly influenced by LHF (Figs. 7–9). The correlations between LHF and local storage are 0.4–0.7, which are significant at the 95% level at 15°N, 38°W and 14.5°N, 51°W (Table 1). The standard deviations of 40–70-day LHF and SST at the three buoy locations are 9–14  $\text{W m}^{-2}$  and 0.1°–0.15°C, respectively, which are similar to those reported on intraseasonal time scales by McPhaden (2002) in the western equatorial Pacific. The amplitudes of the storage and LHF oscillations in the northwestern tropical Atlantic are greatest during boreal fall and winter, when the wind speed oscillations are strongest (Foltz

and McPhaden, 2004), suggesting that the changes in storage are due primarily to wind-induced LHF.

We explicitly assess the causes of LHF variability by considering the LHF perturbed about its seasonal cycle:

$$Q'_e = \rho_a L_e C_e [\overline{W}q'_s - \overline{W}q' + W'(\overline{q}_s - \overline{q})]. \quad (2)$$

Here the prime represents the 40–70-day bandpassed value, and an overbar indicates the seasonal cycle with periods <4 months removed. The first three terms in brackets represent the portion of the intraseasonal LHF due to intraseasonal variations of (from left to

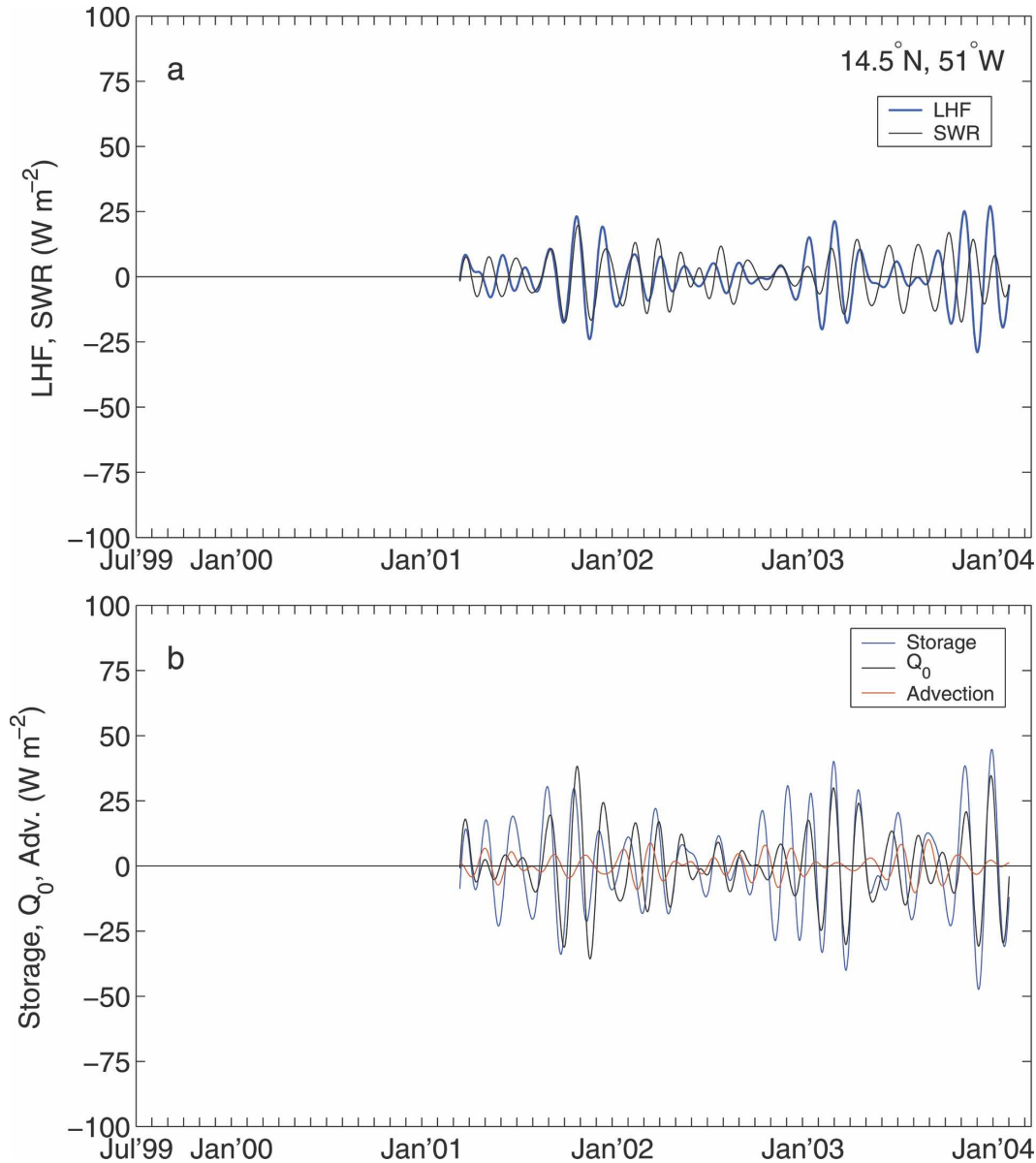


FIG. 8. Same as in Fig. 7, except at  $14.5^{\circ}\text{N}$ ,  $51^{\circ}\text{W}$ .

right) saturation specific humidity (a function of SST), specific humidity, and wind speed. Nonlinear effects, which include terms with a product of two or more primed variables, are small in comparison to the three terms in (2) and can therefore be neglected (each nonlinear term has a standard deviation of  $<0.7 \text{ W m}^{-2}$ ).

At each site, wind speed makes the most important contribution to the LHF (Fig. 10). Standard deviations of the wind-induced LHF ( $Q_w$ ) are similar at all three locations, ranging from 9 to  $12 \text{ W m}^{-2}$ , and the correlation between  $Q_w$  and the total LHF ( $Q_{\text{tot}}$ ) is highly significant (0.8) at each location (Table 2). Specific humidity is on average out of phase with wind speed at

$15^{\circ}\text{N}$ ,  $38^{\circ}\text{W}$  (i.e.,  $q$  is low when  $W$  is high), resulting in a significant positive correlation between humidity-induced LHF ( $Q_q$ ) and  $Q_{\text{tot}}$ . In contrast,  $Q_q$  and  $Q_{\text{tot}}$  are more weakly positively correlated at  $14.5^{\circ}\text{N}$ ,  $51^{\circ}\text{W}$  and  $18^{\circ}\text{N}$ ,  $34^{\circ}\text{W}$ . As a result, intraseasonal LHF variability is the strongest at  $15^{\circ}\text{N}$ ,  $38^{\circ}\text{W}$  even though variations of  $Q_w$  here are the weakest. Latent heat loss due to changes in saturation specific humidity ( $Q_q$ ) is weaker than both  $Q_w$  and  $Q_q$  at each location and is not highly correlated with  $Q_{\text{tot}}$  (Table 2).

With the exception of fall 2001–spring 2002 at  $14.5^{\circ}\text{N}$ , and  $15^{\circ}\text{N}$ ,  $38^{\circ}\text{W}$ , absorbed SWR is poorly correlated with both LHF and local storage (Figs. 7–9), suggesting

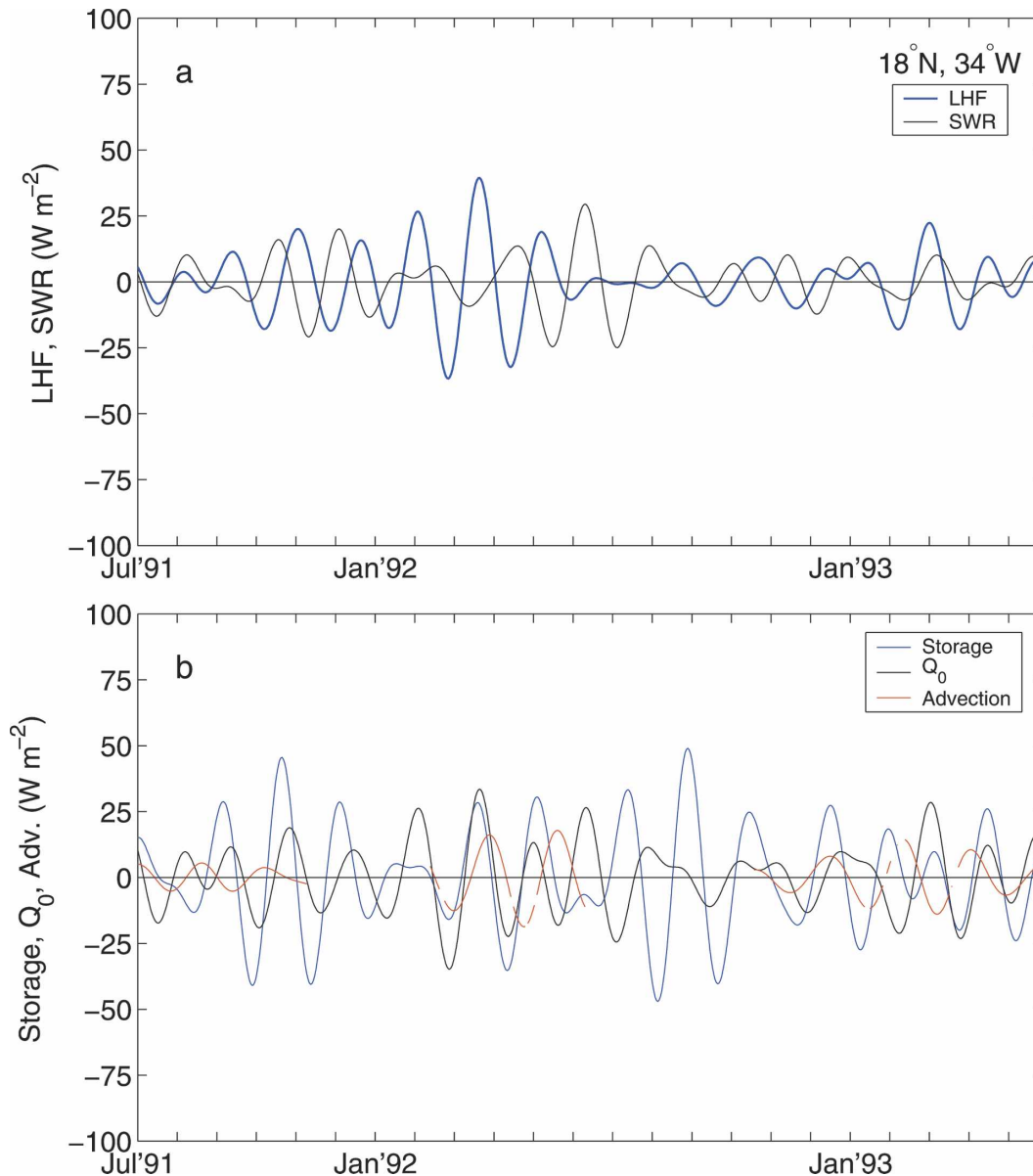


FIG. 9. Same as in Fig. 7, except at  $18^\circ\text{N}$ ,  $34^\circ\text{W}$ .

that the surface wind fluctuations in general are not simply related to changes in cloudiness at these locations.

#### 4. Horizontal advection and entrainment

In this section we consider the terms in the mixed layer heat balance (1) related first to horizontal advection and then to entrainment. We estimate horizontal mixed layer velocity at the Subduction site ( $18^\circ\text{N}$ ,  $34^\circ\text{W}$ ) using direct velocity measurements from the buoy. At the NTAS and PIRATA sites, where direct

velocity measurements are not available, we follow Lagerloef et al. (1999) in assuming that horizontal mixed layer velocity satisfies a linear steady momentum balance,

$$f\hat{\mathbf{k}} \times \mathbf{v} = -gh\nabla\eta + \frac{\tau}{\rho} - r\mathbf{v}_e, \quad (3)$$

where  $\hat{\mathbf{k}}$  is the vertical unit vector,  $\mathbf{v} \equiv \mathbf{v}_g + \mathbf{v}_e$  is the horizontal velocity averaged vertically in the mixed layer ( $\mathbf{v}_g$  and  $\mathbf{v}_e$  are the geostrophic and Ekman components, respectively),  $\eta$  is sea level,  $\tau$  is wind stress (estimated using wind velocity from the buoys), and  $r$  is

TABLE 1. Standard deviations ( $W m^{-2}$ ) of the terms in the mixed layer heat balance (1) and correlation of each term with  $\rho c_p h \partial T / \partial t$  (correlations are in parentheses). The “sum” column represents the sum of LHF, SWR, LWR, sensible heat flux (SHF), and horizontal advection (HA).

	LHF	SWR	LWR	SHF	HA	Sum	$\rho c_p h \partial T / \partial t$
15°N, 38°W	14 (0.7*)	8 (0.3)	3 (-0.1)	1 (0.2)	5 (0.0)	16 (0.8*)	23 (1.0*)
14.5°N, 51°W	9 (0.7*)	8 (0.3)	2 (-0.1)	1 (0.6*)	4 (0.3)	13 (0.8*)	17 (1.0*)
18°N, 34°W	12 (0.4)	9 (-0.1)	2 (-0.1)	1 (0.3)	7 (0.2)	15 (0.5)	20 (1.0*)

\* Significantly different than zero at the 95% level [number of degrees of freedom for the filtered data are estimated following Davis (1976)].

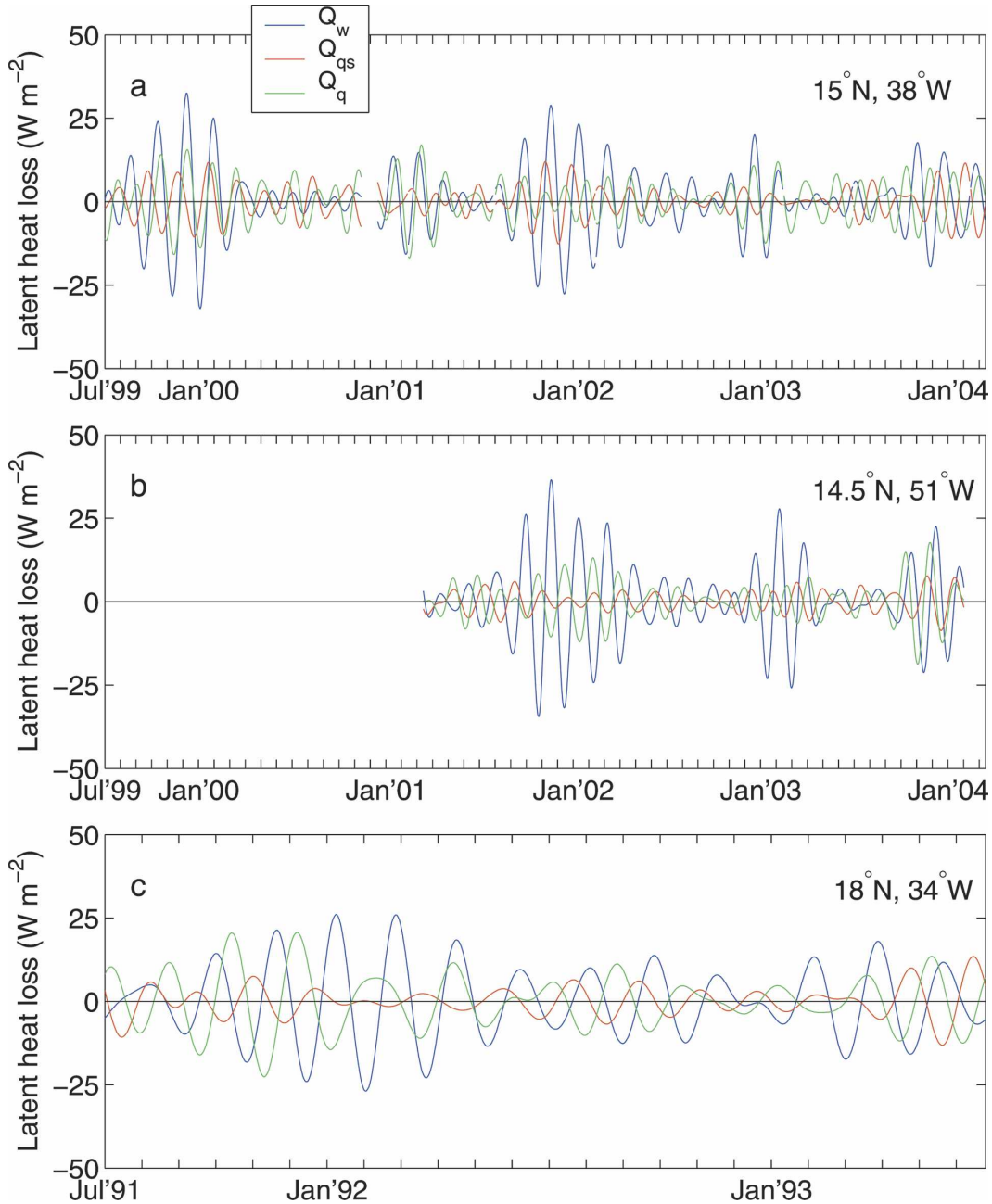


FIG. 10. LHF due to fluctuations of wind speed ( $Q_w$ ), saturation specific humidity ( $Q_{qs}$ ), and specific humidity ( $Q_q$ ) [see (2)] at (a) 15°N, 38°W; (b) 14.5°N, 51°W; and (c) 18°N, 34°W.

TABLE 2. Standard deviations ( $\text{W m}^{-2}$ ) of the terms in the LHF (2);  $Q_w$ ,  $Q_q$ , and  $Q_{qs}$  represent contributions from 40–70-day oscillations of wind speed, specific humidity, and saturation specific humidity, respectively. Shown in parentheses is the correlation of each term with the total 40–70-day LHF ( $Q_{\text{tot}}$ ).

	$Q_w$	$Q_q$	$Q_{qs}$	$Q_{\text{tot}}$
15°N, 38°W	9 (0.8*)	6 (0.6*)	5 (0.2)	14 (1.0*)
14.5°N, 51°W	12 (0.8*)	6 (0.1)	3 (0.0)	9 (1.0*)
18°N, 34°W	11 (0.8*)	8 (0.4)	4 (−0.2)	12 (1.0*)

\* Significantly different than zero at the 95% level [number of degrees of freedom for the filtered data are estimated following Davis (1976)].

a linear drag coefficient. Following Grodsky and Carton (2001) we assign  $r = 2 \times 10^{-4} \text{ m s}^{-1}$ . To estimate horizontal temperature advection, the velocity estimates at 18°N, 34°W are multiplied by Reynolds et al. (2002) SST gradients, and the velocity estimates at 14.5°N, 51°W and 15°N, 38°W are multiplied by TMI horizontal SST gradients. For both datasets, gradients are calculated over a distance of 2° centered on the buoy location. The magnitudes of the record-length mean  $\partial(\text{SST})/\partial x$  and  $\partial(\text{SST})/\partial y$  based on Reynolds et al. (2002) SST gradients are 15%–25% lower than those based on TMI SST, and the standard deviations of 40–70-day Reynolds et al. (2002) SST gradients are ~40% lower than those of the TMI gradients. It is therefore possible that our use of Reynolds et al. (2002) SST gradients leads to an underestimation of intraseasonal temperature advection at 18°N, 34°W.

To estimate uncertainties associated with our estimates of mixed layer velocity at 14.5°N, 51°W and 15°N, 38°W, we have compared the direct ocean current measurements at 18°N, 34°W to estimates from (3). We find that the Ekman component of velocity underestimates the buoy mixed layer velocity by a factor of 5 for the zonal component and by a factor of 10 for the meridional component (based on standard deviations of the 40–70-day bandpassed values). The correlations between the Ekman and buoy velocity are 0.6 for the zonal component (significant at the 95% level), but −0.1 for the meridional component. When the geostrophic component is added to the Ekman component, the correlations with the buoy velocity remain low (0.3 for the zonal component and 0.0 for the meridional component, estimated only for the last 9 months of the record, when sea level data are available). We therefore expect that our estimates of horizontal heat advection at 14.5°N, 51°W and 15°N, 38°W contain a high degree of uncertainty.

Next we consider the role of horizontal advection in the heat balance at each location. Horizontal heat ad-

vection at 18°N, 34°W, where ocean velocity is measured directly at the buoy, is weaker than both LHF and SWR and is weakly correlated with local storage (Table 1; Fig. 9). Horizontal heat advection at 14.5°N, 51°W and 15°N, 38°W is also weak in comparison to LHF and SWR and is not strongly correlated with local storage (Figs. 7, 8).

Despite the anticipated large uncertainties in horizontal advection at 14.5°N, 51°W and 15°N, 38°W, it is nevertheless unlikely that this term plays a dominant role in the heat budget at either location. We base our argument on the results at 18°N, 34°W, where direct measurements of mixed layer velocity are available. Here the correlation between local storage and the sum of terms is unchanged at 0.5 when the modeled Ekman currents are used in the place of the buoy-measured currents to estimate advection, and the standard deviation of the sum of terms is reduced by only  $2 \text{ W m}^{-2}$ . In contrast, the exclusion of LHF from the balance results in a storage sum correlation of only 0.1 and drops the standard deviation of the sum to  $8 \text{ W m}^{-2}$  from  $15 \text{ W m}^{-2}$ . We therefore anticipate that although the magnitude of horizontal advection may be underestimated at the NTAS and PIRATA moorings, it likely does not contribute as significantly to local storage as does LHF. This suggests that on intraseasonal time scales local storage in the northwestern tropical Atlantic is driven primarily by LHF. Previous studies indicate that LHF also contributes significantly to seasonal and longer time-scale SST variability in this region (Carton et al. 1996; Foltz et al. 2003).

Estimation of entrainment requires knowledge of the horizontal mass divergence within the mixed layer and the rate of change of the mixed layer depth ( $w_e = \partial h/\partial t + \nabla \cdot h\mathbf{v}$ ). We calculate the divergence term from (3), estimating wind stress at 15°N, 38°W from QuikSCAT wind velocity and at 18°N, 34°W from SSM/I wind velocity (horizontal gradients are calculated over a distance of 2° centered on the buoy location). We estimate  $\partial h/\partial t$  at 15°N, 38°W and 18°N, 34°W from the corresponding buoy-based estimates of  $h$ . Since neither subsurface temperature nor salinity is available from the NTAS mooring (14.5°N, 51°W), we cannot estimate entrainment at this site. However, at both 15°N, 38°W and 18°N, 34°W,  $w_e < 0$  throughout the length of each data record so that intraseasonal variations of entrainment are zero (entrainment = 0 for  $w_e < 0$ ). It is therefore unlikely that entrainment contributes significantly at 18°N, 34°W.

Finally, we note that the sum of the terms on the right-hand side of (1) explains only 25%–55% of the variance of the local storage at each location. A significant portion of the unexplained variance can likely be

attributed to uncertainties in our estimates of horizontal advection and mixed layer depth. Uncertainties associated with our estimates of horizontal advection at 14.5°N, 51°W and 15°N, 38°W result primarily from our use of a model to estimate horizontal mixed layer velocity. Errors in the mixed layer depth at all locations result from a combination of poor data coverage and our neglect of intraseasonal and interannual mixed layer depth variability. Additional uncertainties result from gaps in the buoy records at 18°N, 34°W. The combination of these uncertainties likely accounts for a significant portion of the unexplained variance at each location.

### 5. Possible coupled air–sea interactions

We have shown that intraseasonal SST variability in the northern tropical Atlantic is driven primarily by wind-induced LHF. In this section we consider the possibility of coupled interactions between the surface wind field and the wind-induced SST. An analog for potential coupled ocean–atmosphere interactions on intraseasonal time scales can be found by considering variability on longer time scales. Chang et al. (2001) argue that on decadal time scales, fluctuations of the meridional SST gradient in the vicinity of the western equatorial Atlantic warm pool (0°–15°N, 50°–30°W; Fig. 11a) force changes in the surface winds, which then reinforce the anomalous SST gradients through wind-induced LHF. The anomalous surface winds and convergence alter the intensity and location of rainfall in the western equatorial Atlantic intertropical convergence zone (ITCZ; Nobre and Shukla 1996).

A coherent pattern of anomalous surface wind convergence and rainfall is also present on intraseasonal time scales in the western equatorial Atlantic (Figs. 11b,c). Anomalously strong trade winds are linked to surface convergence and rainfall over the western equatorial warm pool. The strongest convergence occurs to the north of the climatological ITCZ [defined as the region of high rainfall ( $>4 \text{ mm day}^{-1}$ ) in Fig. 11a], in the region 10°–15°N, 60°–50°W, while the strongest intraseasonal variations in rainfall are located farther to the southeast, where the climatological wind convergence and convection are stronger and the SST is warmer. The spectral distributions of wind convergence and rainfall in the western tropical Atlantic (5°–15°N, 55°–45°W) are consistent with that of wind speed (Fig. 3), with peaks centered in the 50–60-day period range.

It is possible that a coupled interaction occurs on intraseasonal time scales between the surface wind speed and meridional SST gradient to the north of the ITCZ and the surface wind convergence and convec-

tion over the western equatorial Atlantic warm pool. As shown in the previous section, intraseasonal wind speed fluctuations in the northern tropical Atlantic force changes in SST through wind-induced LHF. The meridional gradient of surface wind speed (Figs. 2a,b) results in an anomalous meridional SST gradient to the north of the climatological ITCZ (Fig. 2c). For the case of anomalously strong trade winds, an anomalous southward SST gradient is created that may further increase the strength of the trade winds in the northern tropical Atlantic and the strength of convection over the warm pool. The strengthened winds may in turn result in an amplification of the original anomalous SST gradient.

It is also possible that the intraseasonal oscillations may affect variability on longer time scales. The peak strength of the 40–70-day oscillations occurs in boreal winter (Foltz and McPhaden 2004), one season before the decadal variability associated with the interhemispheric SST gradient reaches its peak. Through their effect on wind convergence and convection to the north of the ITCZ, the wintertime intraseasonal oscillations may set the stage for subsequent springtime anomalies in ITCZ intensity and location. The tropical Pacific offers an analog for this kind of scale interaction wherein air–sea interaction associated with MJO variability rectifies into lower-frequency ENSO fluctuations (Kessler and Kleeman 2000).

### 6. Summary

Through an analysis of the mixed layer heat balance at three locations in the northwestern tropical Atlantic, we have shown that the intraseasonal wind speed oscillations in this region force changes in SST primarily through their effect on latent heat loss. The resultant LHF and SST anomalies are similar in magnitude to the intraseasonal LHF and SST fluctuations of the western equatorial Pacific (McPhaden 2002). Substantial uncertainties in our heat budget analysis result from errors in our estimation of the mixed layer depth, horizontal advection, and entrainment. The installation of current meters and additional salinity sensors in the upper 60 m at the PIRATA site would eliminate some of these uncertainties.

We have also found that intraseasonal fluctuations in the intensity of the northern trade winds are associated with anomalous surface wind convergence and convection over the warm ( $>27^\circ\text{C}$ ) SST of the western equatorial Atlantic. These atmospheric anomalies may be part of a coupled interaction between the anomalous surface atmospheric circulation and the anomalous wind-induced meridional SST gradient. The combina-

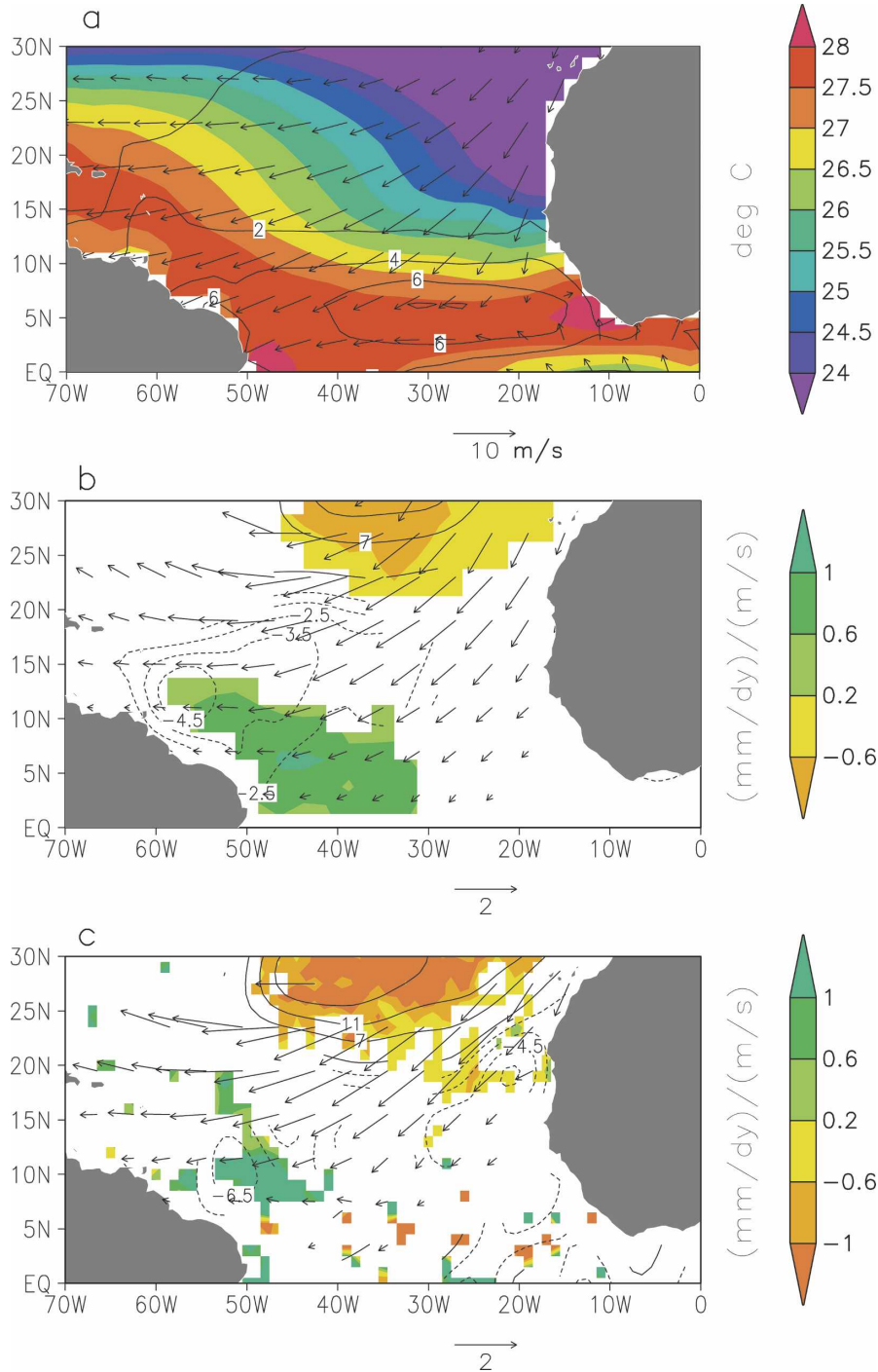


FIG. 11. (a) Annual mean Reynolds et al. (2002) SST (shaded; °C), CMAP rainfall (contours; mm day<sup>-1</sup>), and NCEP-NCAR reanalysis surface winds (1982–2004). (b) Regression of the 40–70-day bandpass-filtered NCEP-NCAR reanalysis surface winds (vectors) and surface wind divergence [contours; 10<sup>-7</sup> s<sup>-1</sup> (m s<sup>-1</sup>)<sup>-1</sup>] and CMAP rainfall [mm day<sup>-1</sup> (m s<sup>-1</sup>)<sup>-1</sup>] onto the 40–70-day NCEP-NCAR reanalysis NATL wind speed index (1982–2004). (c) Regression of 40–70-day QuikSCAT surface winds (vectors) and surface wind divergence [contours; 10<sup>-7</sup> s<sup>-1</sup> (m s<sup>-1</sup>)<sup>-1</sup>] and TRMM rainfall [mm day<sup>-1</sup> (m s<sup>-1</sup>)<sup>-1</sup>] onto the 40–70-day QuikSCAT NATL wind speed index (1999–2004; Fig. 1b shows the NATL index; Fig. 2a shows the NATL index region). Values are shown only where they exceed the 95% confidence level (wind vectors are shown where wind speed exceeds the 95% level).

tion of an anomalous meridional SST gradient to the north of the ITCZ and anomalous convection within the ITCZ is also a well-known feature of interannual and decadal variability in the region. This allows for the possibility of interactions between the intraseasonal fluctuations and these longer time-scale variations.

*Acknowledgments.* We thank Al Pluedemann at the Woods Hole Oceanographic Institution for providing the surface NTAS data and R. A. Weller and R. E. Davis for providing the Subduction data. The NOAA Climate Diagnostics Center provided the NCEP–NCAR reanalysis and CMAP data. The TRMM precipitation data were obtained from the NASA Goddard Space Flight Center. QuikSCAT and SSM/I winds and TOPEX/Poseidon/Jason sea level data were provided by the NASA Jet Propulsion Laboratory. This research was performed while GF held a National Research Council Research Associateship Award at NOAA/PMEL. The authors wish to acknowledge NOAA's Office of Oceanic and Atmospheric Research and Office of Global Programs for support of this research. We also thank two anonymous reviewers for helpful comments.

#### REFERENCES

- Carton, J. A., X. H. Cao, B. S. Giese, and A. M. daSilva, 1996: Decadal and interannual SST variability in the tropical Atlantic Ocean. *J. Phys. Oceanogr.*, **26**, 1165–1175.
- Cayan, D. R., 1992: Latent and sensible heat flux anomalies over the northern oceans: Driving the sea surface temperature. *J. Phys. Oceanogr.*, **22**, 859–881.
- Chang, P., L. Ji, and H. Li, 1997: A decadal climate variation in the tropical Atlantic Ocean from thermodynamic air–sea interactions. *Nature*, **385**, 516–518.
- , —, and R. Saravanan, 2001: A hybrid coupled model study of tropical Atlantic variability. *J. Climate*, **14**, 361–390.
- Cheney, R., L. Miller, R. Agreen, N. Doyle, and J. Lillibridge, 1994: TOPEX/Poseidon: The 2-cm solution. *J. Geophys. Res.*, **99**, 24 555–24 563.
- Ciasto, L. M., and D. W. J. Thompson, 2004: North Atlantic atmosphere–ocean interaction on intraseasonal time scales. *J. Climate*, **17**, 1617–1621.
- Clark, N. E., L. Eber, R. M. Laurs, J. A. Renner, and J. F. T. Saur, 1974: Heat exchange between ocean and atmosphere in the eastern North Pacific for 1961–71. NOAA Tech. Rep. NMRS SSRF-682, National Oceanic and Atmospheric Administration, U.S. Department of Commerce, Washington, DC, 108 pp.
- Cronin, M. F., and M. J. McPhaden, 1997: The upper ocean heat balance in the western equatorial Pacific warm pool during September–December 1992. *J. Geophys. Res.*, **102**, 8533–8553.
- Czaja, A., P. van der Vaart, and J. Marshall, 2002: A diagnostic study of the role of remote forcing in tropical Atlantic variability. *J. Climate*, **15**, 3280–3290.
- Davis, R. E., 1976: Predictability of sea surface temperatures and sea level pressure anomalies over the North Pacific Ocean. *J. Phys. Oceanogr.*, **6**, 249–266.
- Enfield, D. B., and D. A. Mayer, 1997: Tropical Atlantic sea surface temperature variability and its relation to El Niño–Southern Oscillation. *J. Geophys. Res.*, **102**, 929–945.
- Fairall, C. W., E. F. Bradley, D. P. Rogers, J. B. Edson, and G. S. Young, 1996: Bulk parameterization of air–sea fluxes for TOGA COARE. *J. Geophys. Res.*, **101**, 3747–3764.
- Foltz, G. R., and M. J. McPhaden, 2004: The 30–70 day oscillations in the tropical Atlantic. *Geophys. Res. Lett.*, **31**, L15205, doi:10.1029/2004GL020023.
- , S. A. Grodsky, J. A. Carton, and M. J. McPhaden, 2003: Seasonal mixed layer heat budget of the tropical Atlantic Ocean. *J. Geophys. Res.*, **108**, 3146, doi:10.1029/2002JC001584.
- , —, —, and —, 2004: Seasonal salt budget of the northwestern tropical Atlantic Ocean along 38°W. *J. Geophys. Res.*, **109**, C03052, doi:10.1029/2003JC002111.
- Grodsky, S. A., and J. A. Carton, 2001: Intense surface currents in the tropical Pacific. *J. Geophys. Res.*, **106**, 16 673–16 684.
- Kalnay, E., and Coauthors, 1996: The NCEP/NCAR 40-Year Reanalysis Project. *Bull. Amer. Meteor. Soc.*, **77**, 437–471.
- Kessler, W. S., and R. Kleeman, 2000: Rectification of the Madden–Julian oscillation into the ENSO cycle. *J. Climate*, **13**, 3560–3575.
- Lagerloef, G. S. E., G. T. Mitchum, R. B. Lukas, and P. P. Niiler, 1999: Tropical Pacific near-surface currents estimated from altimeter, wind, and drifter data. *J. Geophys. Res.*, **104**, 23 313–23 326.
- Levitus, S., and T. Boyer, 1994: *Temperature*. Vol. 4, *World Ocean Atlas 1994*, NOAA Atlas NESDIS 4, 129 pp.
- , R. Burgett, and T. Boyer, 1994: *Salinity*. Vol. 3, *World Ocean Atlas 1994*, NOAA Atlas NESDIS 3, 111 pp.
- Liu, W. T., W. Tang, and P. S. Polito, 1998: NASA scatterometer provides global ocean surface wind fields with more structures than numerical weather prediction. *Geophys. Res. Lett.*, **25**, 761–764.
- McPhaden, M. J., 2002: Mixed layer temperature balance on intraseasonal timescales in the equatorial Pacific Ocean. *J. Climate*, **15**, 2632–2647.
- Medovaya, M. D., D. E. Waliser, R. A. Weller, and M. J. McPhaden, 2002: Assessing ocean buoy shortwave observations using clear-sky model calculations. *J. Geophys. Res.*, **107**, 3014, doi:10.1029/2000JC000558.
- Moisan, J. R., and P. P. Niiler, 1998: The seasonal heat budget of the North Pacific: Net heat flux and heat storage rates (1950–1990). *J. Phys. Oceanogr.*, **28**, 401–421.
- Monterey, G. I., and S. Levitus, 1997: *Seasonal Variability of Mixed Layer Depth for the World Ocean*. NOAA Atlas NESDIS 14, 5 pp. and 87 figs.
- Moyer, K. A., and R. A. Weller, 1997: Observations of surface forcing from the Subduction Experiment: A comparison with global model products and climatological datasets. *J. Climate*, **10**, 2725–2742.
- Nobre, C., and J. Shukla, 1996: Variations of sea surface temperature, wind stress, and rainfall over the tropical Atlantic and South America. *J. Climate*, **9**, 2464–2479.
- Pailler, K., B. Bourles, and Y. Gouriou, 1999: The barrier layer in the western tropical Atlantic Ocean. *Geophys. Res. Lett.*, **26**, 2069–2072.
- Reed, R., 1977: On estimating insolation over the ocean. *J. Phys. Oceanogr.*, **7**, 482–485.
- Reynolds, R. W., N. A. Rayner, T. M. Smith, D. C. Stokes, and W. Q. Wang, 2002: An improved in situ and satellite SST analysis for climate. *J. Climate*, **15**, 1609–1625.
- Rio, M.-H., and F. Hernandez, 2004: A mean dynamic topography

- computed over the world ocean from altimetry, in-situ measurements, and a geoid model. *J. Geophys. Res.*, **109**, C12032, doi:10.1029/2003JC002226.
- Servain, J., A. J. Busalacchi, M. J. McPhaden, A. D. Moura, G. Reverdin, M. Vianna, and S. E. Zebiak, 1998: A Pilot Research Moored Array in the Tropical Atlantic (PIRATA). *Bull. Amer. Meteor. Soc.*, **79**, 2019–2031.
- Sprintall, J., and M. Tomczak, 1992: Evidence of the barrier layer in the surface layer of the tropics. *J. Geophys. Res.*, **97**, 7305–7316.
- Stevenson, J. W., and P. P. Niiler, 1983: Upper ocean heat budget during the Hawaii-to-Tahiti shuttle experiment. *J. Phys. Oceanogr.*, **13**, 1894–1907.
- Swenson, M. S., and D. V. Hansen, 1999: Tropical Pacific Ocean mixed layer heat budget: The Pacific cold tongue. *J. Phys. Oceanogr.*, **29**, 69–81.
- Waliser, D. E., R. A. Weller, and R. D. Cess, 1999: Comparisons between buoy-observed, satellite-derived, and modeled surface shortwave flux over the subtropical North Atlantic during the Subduction Experiment. *J. Geophys. Res.*, **104**, 31 301–31 320.
- Wang, W. M., and M. J. McPhaden, 1999: The surface-layer heat balance in the equatorial Pacific Ocean. Part I: Mean seasonal cycle. *J. Phys. Oceanogr.*, **29**, 1812–1831.
- Wentz, F. J., 1997: A well-calibrated ocean algorithm for special sensor microwave/imager. *J. Geophys. Res.*, **102**, 8703–8718.
- Xie, S.-P., and Y. Tanimoto, 1998: A pan-Atlantic decadal climate oscillation. *Geophys. Res. Lett.*, **25**, 2185–2188.